A highly thermal stable cubic-phase $Sc(PO_3)_3$:Cr^{3+} phosphor with emitting peak at 875 nm

Le Liu[1,2,3], Wendong Nie[1,3], Huijie Wu[1,3], Jingrong Zhang[1,2,3], Sisi Liang[1,3] and Haomiao Zhu[1,2,3*]

ABSTRACT The compact size and high efficiency of near-infrared (NIR) phosphor-converted light-emitting diodes (pc-LEDs) make them promising light sources in various fields, such as miniature NIR spectrometer. However, the current state of NIR phosphors with emission wavelengths exceeding 850 nm shows poor photoluminescence (PL) thermal stability. In this work, we present cubic-phase $Sc(PO_3)_3$:xCr^{3+} (x = 0, 1, 5, 10, 12, 14, 16 and 18 at%) phosphors that exhibit broadband emission ranging from 725 to 1150 nm, with a peak at 875 nm. Particularly, the PL intensity of the 5 at% sample retains 73.4% of its value at room temperature when measured at 423 K, exhibiting exceptional thermal stability compared with previously reported phosphors with emission peaks exceeding 850 nm. Through a comparison investigation on the variable-temperature X-ray diffraction patterns of cubic- and monoclinic-phase $Sc(PO_3)_3$:Cr^{3+} phosphors, it was revealed that achieving good PL thermal stability in the cubic-phase phosphor may be attributed to the minimal bond length and bond angle variations at elevated temperatures. The fabricated NIR pc-LEDs, driven with a 150-mA current, produce an NIR radiant flux of 26.62 mW. The highest electro-optical conversion efficiency is 11.87% under a drive current of 10 mA. This work provides insights for the discovery of Cr^{3+} ion-doped NIR phosphors with excellent PL thermal stability.

Keywords: near infrared phosphor, pc-LEDs, broadband emission, $Sc(PO_3)_3$, luminescent materials

INTRODUCTION

Near-infrared (NIR) spectroscopy offers numerous advantages, such as high penetration depth and non-invasive monitoring capabilities for biological tissues [1–3]. This technique finds extensive applications in the fields of bio-imaging, night vision, food analysis, and sensors [4–8]. Tungsten halogen lamps, commonly used as NIR light sources, are deemed unsuitable for emerging applications due to their bulky size, low efficiency, and short service lifetime [9,10]. Another option is the NIR diode chips, which are characterized by its small size and high efficiency [11,12]. However, their practical applications are limited due to their relatively high cost and narrow emission bands [6]. In recent years, there has been a growing interest in NIR phosphor-converted light-emitting diodes (pc-LEDs) based on commercially available low-cost blue light chips. These pc-LEDs exhibit high efficiency, broad emission bands, spectral tunability, and long service lifetime [13]. Therefore, it is imperative to develop high-performance broadband NIR phosphors that can be readily excited by blue light.

Currently, Cr^{3+} ion is considered as a promising activator for generating broadband NIR emission [9,13,14]. The luminescence of Cr^{3+} ions, with a $3d^3$ electronic configuration, is strongly influenced by the crystal fields. For instance, they can exhibit broadband emission of the $^4T_{2g}(F) \rightarrow {}^4A_{2g}(F)$ spin-allowed transition in weak crystal fields and sharp line emission of the $^2E_g(G) \rightarrow {}^4A_{2g}(F)$ spin-forbidden transition in strong crystal fields [15,16]. Additionally, Cr^{3+} ions can be excited by cost-effective commercial blue or red LEDs. Consequently, a large number of Cr^{3+} ion-activated inorganic phosphors have been reported in recent years. For instance, Liu's group [17] reported a garnet-structured $Ca_3Sc_2Si_3O_{12}$:Cr^{3+} phosphor that exhibited a broadband emission peaked at 770 nm, achieving a high internal photoluminescence quantum yield (PLQY) of 92.3% and excellent PL thermal stability (97.4%@423K). We previously reported the AlP_3O_9:Cr^{3+} phosphor, which exhibits a emission peak at 780 nm, possessing a high internal PLQY of 76% and excellent PL thermal stability (91%@423K), due to near-zero thermal expansion of the host [18]. However, the emission spectra of these phosphors only partially cover the response wavelength range of silicon-based photodetectors, which typically have a long wavelength limit of 1100 nm [19,20]. Other phosphors with longer emission wavelengths, such as $GaTaO_4$:Cr^{3+} (840 nm, 60%@423K) [21], $Mg_4Ta_2O_9$:Cr^{3+} (842 nm, 55%@373K) [22], $Sc(PO_3)_3$:Cr^{3+} (900 nm, 30%@423K) [23], $LaSc_3B_4O_{12}$:Cr^{3+} (871 nm, 24%@423K) [24], and $LiScP_2O_7$:Cr^{3+} (880 nm, 42%@373K) [25], exhibit poor PL thermal stability. Therefore, the development of high thermally stable broadband NIR phosphors with long peak wavelengths (>850 nm) remains a formidable challenge [3].

The $Sc(PO_3)_3$ crystal has two distinct phases, namely a cubic phase with a space group of $I\text{-}43d$ (hereafter referred as CSPO) and a monoclinic phase with a space group of Cc (hereafter referred as MSPO) [26]. Previously published work has shown that the 10 at% Cr^{3+}-doped MSPO phosphor possesses an internal PLQY of 16% and retains 42% of its PL intensity at

[1] CAS Key Laboratory of Design and Assembly of Functional Nanostructures, Fujian Key Laboratory of Nanomaterials, Fujian Institute of Research on the Structure of Matter, Chinese Academy of Sciences, Fuzhou 350002, China
[2] College of Chemistry and Materials Science, Fujian Normal University, Fuzhou 350007, China
[3] Xiamen Key Laboratory of Rare Earth Photoelectric Functional Materials, Xiamen Research Center of Rare Earth Materials, Haixi Institute, Chinese Academy of Sciences, Xiamen 361021, China
* Corresponding author (email: zhm@fjirsm.ac.cn)

room temperature when the temperature is increased to 373 K [23]. It is intriguing to investigate the spectral properties of Cr^{3+}-doped CSPO phosphors and compare them with those of Cr^{3+}-doped MSPO phosphors, especially focusing on the influence of local structure surrounding Cr^{3+} ions on the PL thermal stability of phosphors.

In this study, we present the synthesis and characterization of the cyclotetraphosphate CSPO:xCr^{3+} (x = 0, 1, 5, 10, 12, 14, 16 and 18 at%) NIR phosphor. This phosphor demonstrates a broad emission band spanning from 725 to 1150 nm with the emission peak at 875 nm. Notably, the 14 at% CSPO:Cr^{3+} phosphor exhibits outstanding PL thermal stability (64.6%@423K), surpassing the majority of currently reported NIR phosphors with emission peak exceeding 850 nm. The structural integrity of the [ScO$_6$] octahedra in the CSPO:Cr^{3+} phosphor was evaluated through *in situ* variable-temperature X-ray diffraction (XRD) experiments at room temperature and 423 K. The results revealed minimal distortions in bond lengths and bond angles, confirming its exceptional structural rigidity at elevated temperatures. To demonstrate the practical application of the phosphor, NIR pc-LEDs were fabricated by combining the 14 at% CSPO:Cr^{3+} phosphor with a commercial blue LED chip. This NIR pc-LED exhibited an NIR output power of 26.62 mW at a drive current of 150 mA.

EXPERIMENTAL SECTION

Materials and preparation

Synthesis of cubic-phase CSPO:xCr^{3+} phosphor
The synthesis of cubic-phase CSPO:xCr^{3+} phosphors with different doping concentrations were carried out in two steps using a high-temperature solid-phase reaction method. The used raw materials included Sc$_2$O$_3$ (99.9%, Adamas), Cr$_2$O$_3$ (99.95%, Aladdin), and (NH$_4$)H$_2$PO$_4$ (99%, Aladdin). The (NH$_4$)H$_2$PO$_4$ was weighed with an additional 20% in order to compensate for losses at elevated temperatures. Other raw materials were accurately weighed according to the chemical composition of phosphor samples. Additionally, 1 wt% Li$_2$CO$_3$ (99.99%, Aladdin) and 2 wt% H$_3$BO$_3$ (AR, Aladdin) were added as fluxes. The mixtures were thoroughly ground in an agate mortar. Subsequently, the ground mixture was loaded into a corundum crucible and placed in a muffle furnace. The temperature was slowly increased to 400°C, then to 700°C, and finally to 1100°C, and held for 1 h. The mixture was then removed, finely ground, and reintroduced into the muffle furnace for calcination at 1100°C for 24 h. After being cooled to room temperature, the samples were reground for further measurements.

Synthesis of monoclinic-phase MSPO:xCr^{3+} phosphor
The synthesis of monoclinic-phase MSPO:xCr^{3+} (x = 0 and 10 at%) phosphors was also carried out using the high-temperature solid-phase reaction method. The weighed raw materials were ground in an agate mortar, then placed in an oven and maintained at 190°C for 3 h. Subsequently, they were transferred to a muffle furnace and calcined at 650°C for 8 h. The final sample was obtained by regrinding the cooled product.

Characterization
Powder XRD patterns of the CSPO:Cr^{3+} samples were measured using an X-ray diffractometer (MiniFlex600-C, Rigaku) with Cu

Kα radiation (λ = 0.154059 nm). The measurements were taken at an interval of 0.02° with a speed of 10° min^{-1}. *In situ* variable temperature XRD measurements were conducted on a benchtop X-ray diffractometer (Bruker D8 Advance) with Cu Kα$_1$ radiation. The Rietveld refinement analysis was performed using Fullprof software. The sample morphology was characterized using field emission scanning electron microscopy (SEM, Apreo S LoVac). Diffuse reflectance spectra were recorded using an ultraviolet (UV)-visible-NIR spectrophotometer (Cary 5000) with BaSO$_4$ as the reference. Steady-state excitation spectra, emission spectra, and PL lifetime curves were recorded using an FLS980 fluorescence spectrometer (Edinburgh Instruments) equipped with a xenon lamp (450 W). For the PL decay curves measurement, an OPO pulsed laser (NT242, EKSPLA) was used as the light source. Temperature-dependent emission spectra were recorded using the same spectrometer along with a THMS 600 temperature control stage (Linkam Scientific Instruments).

LED packaging
The NIR pc-LED was packaged by combining the CSPO:Cr^{3+} (14 at%) phosphor with a commercially available 480 nm blue diode chip. Firstly, silicone A and B are mixed in a 1:1 ratio, followed by addition of phosphors. Through our experimental investigations, we have determined that the optimal weight ratio for mixing phosphor and silicone is 1:1. The resulting mixture was then coated onto the blue diode chip and dried in an oven at 120°C for 2 h to produce the NIR pc-LED.

RESULTS AND DISCUSSION

Crystal structure and phase identification
The cubic-phase CSPO crystal belongs to cyclotetraphosphate and has a space group of I-43d [26]. This compound consists of [ScO$_6$] octahedra and [PO$_4$] tetrahedra, in which Sc^{3+} and P^{5+} ions are coordinated with six and four O atoms, respectively (Fig. 1a). The [ScO$_6$] and [PO$_4$] are connected through shared angular O atoms, forming a larger octahedral framework, while the [PO$_4$] are interconnected to create a tetrakisphosphate ring structure. Considering the comparable effective radii (Sc^{3+}: R = 0.75 Å, coordination number (CN) = 6; Cr^{3+}: R = 0.62 Å, CN = 6) [27], the same valence and CN of Sc^{3+} and Cr^{3+} ions, we propose that the doped Cr^{3+} ions will occupy the sites of Sc^{3+} ions in the CSPO host.

Fig. 1b illustrates the XRD patterns of CSPO:xCr^{3+} (x = 0–18 at%) phosphors at room temperature. The diffraction peaks of all samples precisely match the standard pattern of CSPO (PDF#30-1123), indicating the absence of any impurity phases. With increasing doping concentration of Cr^{3+} ions, the diffraction peaks exhibit a shift towards higher angles. This shift indicates the successful incorporation of Cr^{3+} ions, due to the smaller ionic radii of Cr^{3+} as compared with that of Sc^{3+} ions. The Rietveld refinement of the CSPO:Cr^{3+} (14 at%) and CSPO samples are depicted in Fig. 1c and Fig. S1, demonstrating excellent convergence. The refined crystallographic data are provided in Tables S1 and S2. The results reveal a reduction in cell size, which is consistent with the observed shift of the diffraction peaks towards higher 2θ angles as revealed by XRD analysis.

SEM images of the CSPO:Cr^{3+} (14 at%) sample shows irregularly shaped phosphor grains with sizes ranging from 5 to 20 μm (Fig. 1d). The EDS mapping of randomly selected CSPO:
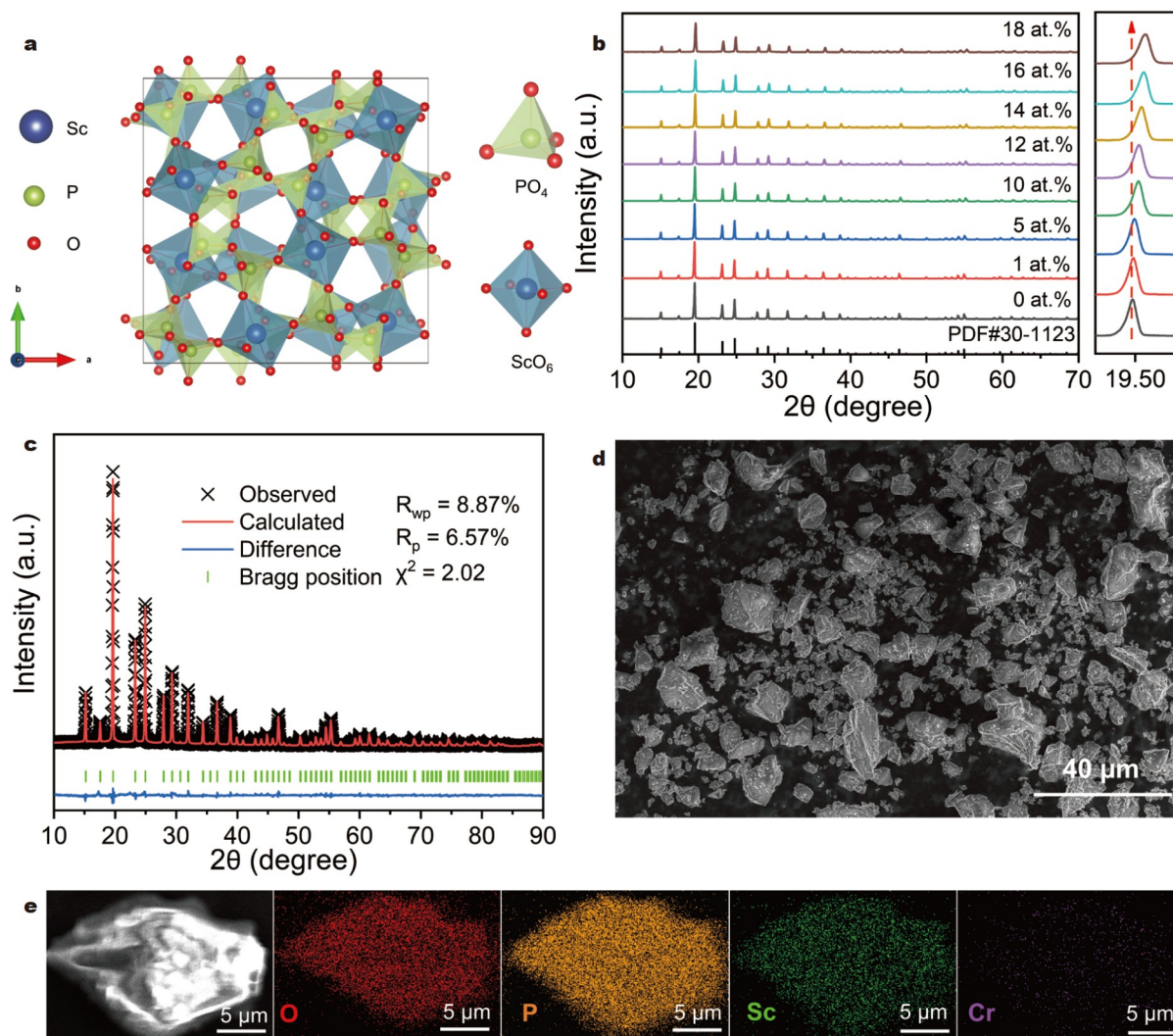
Figure 1 (a) Crystal structure of CSPO. (b) XRD patterns of CSPO:xCr^{3+} (x = 0–18 at%) samples and magnified patterns in the range of 19° to 20°. (c) Rietveld refinement on the XRD pattern of the CSPO:Cr^{3+} (14 at%) sample. (d) SEM and (e) EDS elemental mapping images of the CSPO:Cr^{3+} (14 at%) sample.

Cr^{3+} particles reveals that P, O, Sc, and Cr elements are uniformly distributed within the particles (Fig. 1e).

Luminescence properties

Fig. S2a, c display the UV-visible-NIR diffuse reflectance spectra of the CSPO:xCr^{3+} (x = 0–18 at%) and MSPO samples, respectively. The deduced bandgaps of undoped CSPO and MSPO crystals are approximately 4.24 and 4.16 eV, respectively (Fig. S2b, d) [34]. Generally, there are primarily two mechanisms for PL thermal quenching: thermal ionization and crossover process [19]. The wide bandgaps of both CSPO and MSPO crystals may possess high energy barriers to impede thermal ionization [35–37]. In another words, the difference between the PL thermal quenching behavior of CSPO:Cr^{3+} and MSPO:Cr^{3+} phosphors are mainly related to the crossover process in these two phosphors. In the doped samples, two broad absorption bands are observed, centered at 490 and 730 nm, corresponding to the $^4A_{2g}(F) \rightarrow {}^4T_{1g}(F)$ and $^4A_{2g}(F) \rightarrow {}^4T_{2g}(F)$ transitions of Cr^{3+} ions, respectively. Additionally, the presence of a weak absorption band peaked at around 670 nm can be attributed to the Fano antiresonance phenomenon [38,39]. This phenomenon

arises from the spin-orbit interaction between the $^2E_g(G)$ and $^4T_{2g}(F)$ energy levels of the Cr^{3+} ion, which is also observed in the excitation spectrum (Fig. 2a).

The excitation and emission spectra of the CSPO:Cr^{3+} (14 at%) sample are depicted in Fig. 2a, with the excitation spectrum aligning well with the diffuse reflectance spectrum. Upon excitation at a wavelength of 490 nm, a broad emission band spanning from 725 to 1150 nm was observed, with a peak at 875 nm and a full width at half maximum (FWHM) of approximately 140 nm. It is worth noting that the emission of this phosphor exceeds 1000 nm, which is the long wavelength response limit of the external photomultiplier tube (EXT Red PMT, 200–1000 nm). To obtain the complete emission spectrum, an additional NIR PMT (950–1700 nm) was used to measure the emission spectrum in the range of 950–1200 nm. Finally, the emission spectrum was obtained by jointing these two spectra at 950 nm (the dashed vertical line in Fig. 2a). The Tanabe–Sugan diagram is often used to describe the relationship between the energy level position of Cr^{3+} and the crystal field, as shown in Fig. 2b. The energies of $^4T_{1g}(F)$, $^4T_{2g}(F)$, and $^2E_g(G)$ states of the Cr^{3+} ions were determined based on the experi-
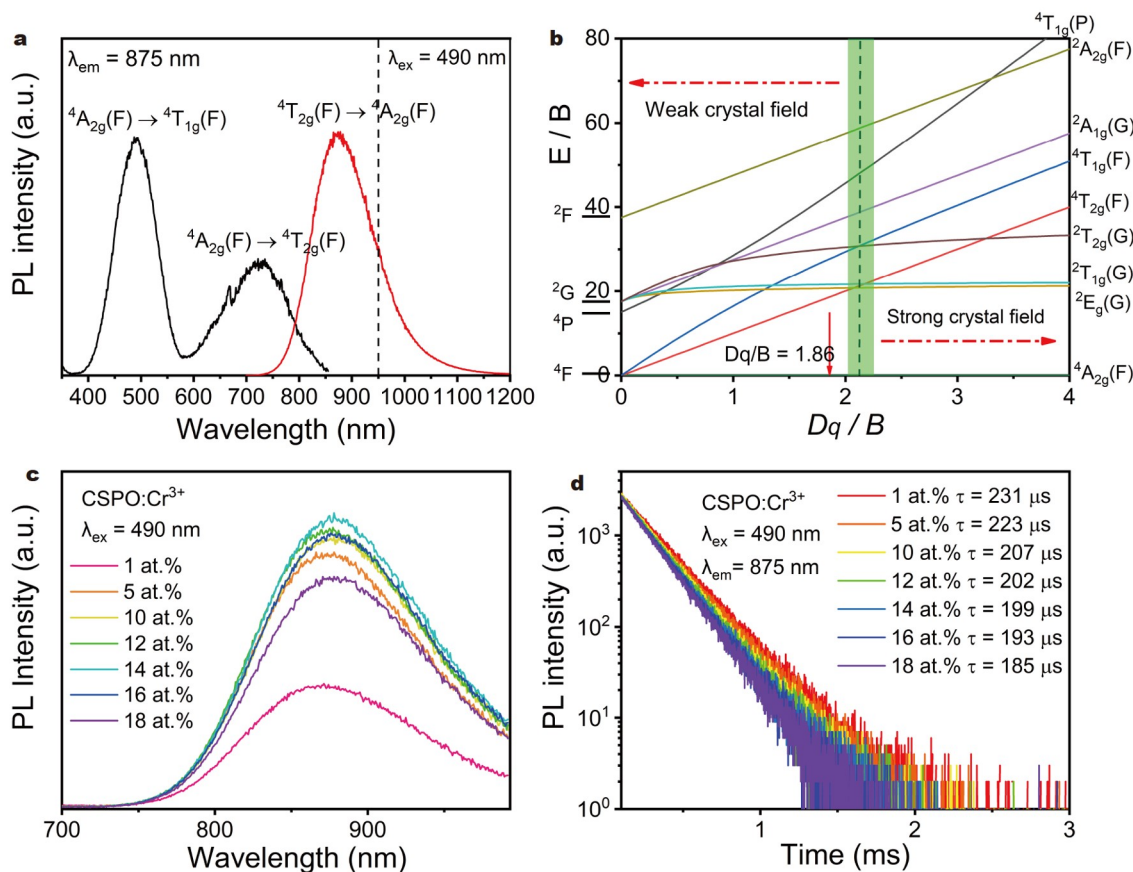
Figure 2 (a) Excitation and emission spectra of the CSPO:Cr^{3+} (14 at%) sample. The emission spectrum is composed of 700–950 and 950–1200 nm range, which are detected using the EXD Red PMT and NIR PMT detector, respectively. (b) Tanabe–Sugan energy diagram of the 3d^3 system in octahedral crystal field. (c) PL spectra and (d) PL decay curves (excited at 490 nm, monitored at 875 nm) of CSPO:xCr^{3+} (x = 1–18 at%).

mental data. The D_q/B ratio was calculated to be approximately 1.86 (see the Supplementary information), indicating a weak crystal field environment for the Cr^{3+} ion [40,41]. Consequently, only the broad radiative transition from $^4T_{2g}(F)$ to $^4A_{2g}(F)$ state was observed.

The emission spectra of CSPO:xCr^{3+} (x = 1–18 at%) samples are presented in Fig. 2c. It is evident that the luminescence intensity increases as the Cr^{3+} concentration increases, reaching its maximum at 14 at%, with an internal PLQY of 40.5% and an external PLQY of 18.4%. However, as the Cr^{3+} concentration continues to increase, the luminescence intensity decreases due to concentration quenching. The highest internal PLQY among all the samples was approximately 49.7% for the 5 at% doped sample, while the highest external PLQY was 18.4% for the 14 at% doped sample, as shown in Fig. S3a. Fig. S3b shows the spectral data for calculating the internal PLQY of the 14 at% sample. Additionally, PL decay curves were obtained by monitoring the emission at 875 nm (Fig. 2d). All the curves exhibited monoexponential decay, and a fluorescence lifetime of approximately 199 μs was fitted for a Cr^{3+} ion doping concentration of 14 at%. With increasing Cr^{3+} doping concentration, the fluorescence lifetime shortened, indicating the occurrence of concentration quenching [42].

PL thermal stability
The PL thermal stability of NIR phosphors is crucial in determining their value for application, as the temperature of NIR pc-

LEDs tends to be high during operation. To assess this, the temperature-dependent emission spectra of the samples with different Cr^{3+} doping concentrations (x = 1, 5 and 14 at%) were recorded in the temperature range of 298 to 448 K (Fig. 3a–c). With increasing temperature, the emission spectra exhibit a slight red shift, probably attributed to lattice expansion [13,43]. The normalized PL intensity *versus* temperature is shown in Fig. 3d, demonstrating a decrease in the integrated emission intensity as the temperature rises. The retained integrated PL intensities at 423 K are 77.2%, 73.4%, 64.6% for the 1, 5 and 14 at% doped samples, respectively. Obviously, the PL thermal stability is declined with enhancing Cr^{3+} concentration. This phenomenon can be explained by the fact that higher Cr^{3+} doping may cause more crystallographic structural defects in the host, which will quench the luminescence, especially at elevated temperatures. Moreover, the high Cr^{3+} concentration promotes the energy migration among neighboring Cr^{3+} ions, thus inducing more pronounced PL quenching. The spectral characteristics of recently published Cr^{3+}-doped phosphors with emission peaks exceeding 850 nm are summarized in Table 1. As we can see, the CSPO:Cr^{3+} (5 at%) phosphor exhibits outstanding PL thermal stability and relatively high emission efficiency. Although increasing the doping concentration to 14 at% results in a slight decrease in thermal stability, it still surpasses the majority of Cr^{3+} ion-doped phosphors with emission peaks greater than 850 nm.
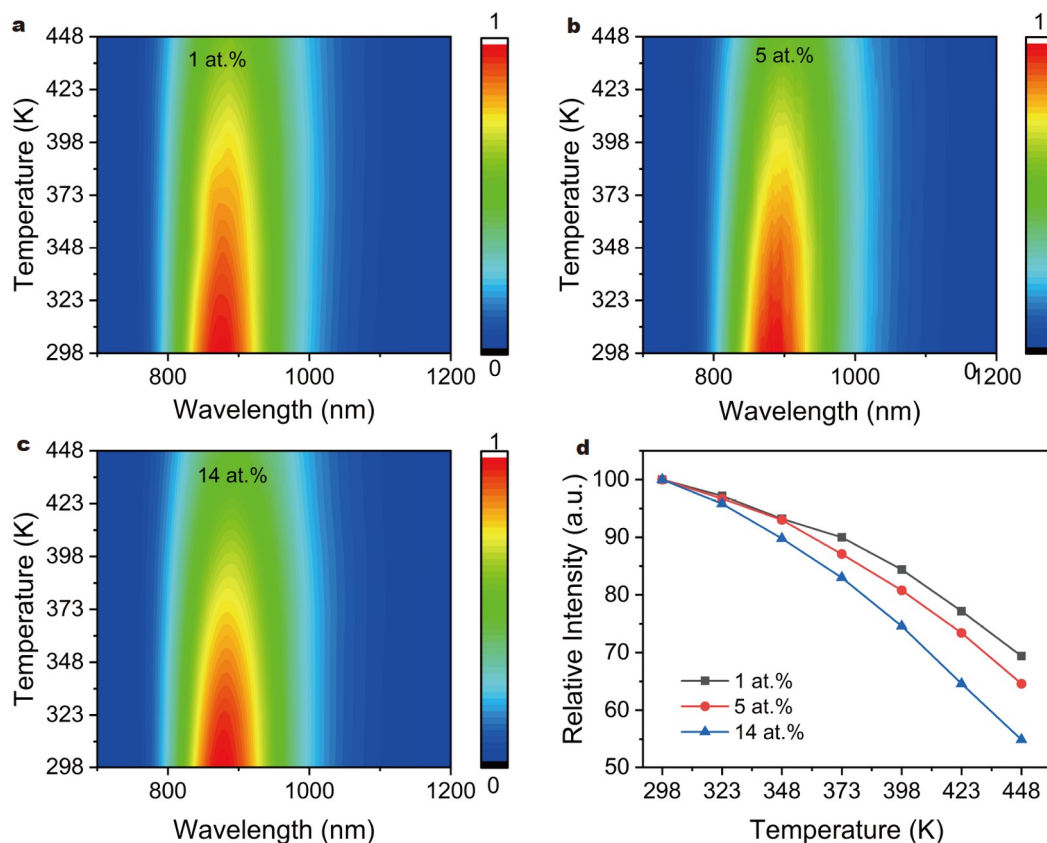
Figure 3 (a–c) Temperature-dependent PL spectra of CSPO:Cr^{3+} (1 at%), CSPO:Cr^{3+} (5 at%) and CSPO:Cr^{3+} (14 at%) samples. (d) Integrated PL intensity *versus* temperature.

Table 1 Several key optical parameters of Cr^{3+}-activated phosphors (peak wavelength > 850 nm)

Phosphor	λ_{ex} (nm)	λ_{em} (nm)	Internal/external PLQY (%)	I_{423K}/I_{298K} (%)	FWHM (nm)	Ref.
CSPO:Cr^{3+}(5 at%)	490	875	49.7/16.5	73.4	140	This work
CSPO:Cr^{3+}(14 at%)	490	875	40.5/18.4	64.6	140	This work
Ga_4GeO_8:Cr^{3+}	430	850	60/27	56.0	215	[28]
$Sr_9Ga(PO_4)_7$:Cr^{3+}	485	850	66.3/29.9	~0	–	[29]
ScF_3:Cr^{3+}	468	852	45/–	85.5	140	[30]
$GaTa_{0.5}Nb_{0.5}O_4$:Cr^{3+}	476	865	94.0/49.4	22.02	145	[31]
$LiScP_2O_7$:Cr^{3+}	470	880	38/20	~20.0	170	[25]
$LiScGe_2O_6$:Cr^{3+}	480	886	72.6/39.9	~41.9	160	[32]
Sr_2ScSbO_6:Cr^{3+}	550	890	82.0/35.7	66.4	190	[33]
$Sc(PO_3)_3$:Cr^{3+}	480	900	16.1/–	~20.0	161	[23]

Octahedral distortion at high temperatures

It is recognized that, besides the thermal ionization mechanism, the thermal quenching of NIR phosphors is predominantly influenced by the host lattice, specifically by bond length and bond angle distortions at elevated temperatures [44,45]. In order to investigate the correlation between local structural distortions nearby Cr^{3+} ions and their luminescent properties at high temperatures, *in situ* variable temperature XRD tests were conducted on the samples at 298 and 423 K. For comparison, the same tests were carried out on the monoclinic MSPO phosphor.

It is worth noting that both MSPO and CSPO crystals have the same composition, differing solely in terms of their crystal structure. The obtained XRD patterns were subjected to Rietveld refinement, and the refined results are presented in Fig. S4. The corresponding detailed crystal structure data of these two phosphors at 298 and 423 K, are summarized in Tables S3 and S4.

We first discuss the bond length distortion of the [ScO_6] octahedral lattice, which can be expressed by the equation: [41,45,46]

$$D = \frac{1}{n} \sum_{i=1}^{n} \left(\frac{|L_i - \overline{L}|}{\overline{L}} \right), \tag{1}$$

where D represents the bond length distortion, L_i represents the bond length from the ith ligand oxygen atom to the central Sc atom, and $\overline{L}$ represents the average Sc–O bond length. The calculated results of the CSPO:Cr^{3+} (14 at%) sample are presented in Table S5, showing that the D value of [ScO$_6$] octahedra increases from 4.22% to 4.82% with an increase in temperature from 298 to 423 K. This indicates a minimal change in bond lengths at elevated temperatures. In contrast, for the MSPO:Cr^{3+} (10 at%) sample, the three [ScO$_6$] octahedra exhibit D values of 9.67%, 5.49%, and 9.57% at 298 K and 10.27%, 10.35%, and 7.91% at 423 K respectively, suggesting a significant change in the bond length at high temperatures.

Meanwhile, bond angle distortion is also a crucial factor that influences the PL thermal stability. The extent of bond angle distortion can be quantified by the bond angle variance, which can be calculated using the following equation [44,47]:

$$\sigma^2 = \frac{1}{11} \sum_{i=1}^{12} (\Phi_i - 90)^2, \tag{2}$$

where σ^2 represents the bond angle variance, Φ_i represents the ith bond angle, and 90° is the ideal bond angle for an octahedron. The results presented in Tables S3–S5 show that, as compared with the monoclinic-phase sample, the cubic-phase sample demonstrates much smaller bond length and bond angle variations between room temperature and 423 K. Recent research pointed out that the shift of the activator environment distribution at room temperature and high temperature is a more precise descriptor for predicting the PL thermal stability of Ce^{3+} and Eu^{2+}-doped phosphors [48–50]. Namely, the smaller the change in the local environment around the activator ions between room and high temperature, the better the PL thermal stability [51]. This may be the primary reason for the excellent thermal stability of CSPO:Cr^{3+} phosphor. Moreover, in the cubic phase, the [ScO$_6$] octahedron is closer to a regular octahedron. Several investigations have shown that Cr^{3+} ions situated in this kind of site possess better PL thermal stability [29,52–54].

NIR pc-LED performance and applications

To demonstrate the device performance of CSPO:Cr^{3+} phosphor, we fabricated two NIR pc-LEDs by combining commercial 480 nm LED chips with CSPO:xCr^{3+} (x = 5 and 14 at%) phosphors, respectively. The electroluminescence spectrum of the pc-

LED (based on the 14 at% phosphor), driven by a 100-mA current, is depicted in Fig. 4a, exhibiting blue emissions at 480 nm and a broadband NIR emission ranging from 725 to 1100 nm, with a peak at 875 nm. Increasing the driving current from 10 to 150 mA (Fig. 4b) resulted in an increase in NIR output power from 3.04 to 26.62 mW, while the electro-optical conversion efficiency decreased from 11.87% to 5.52%. Generally, with increasing driving current, the efficiency of the blue diode chip itself will decline gradually. To show this, we further tested the electro-optical conversion efficiency of the blue diode chip used for fabricating the pc-LED, as shown in Fig. S5a. When the current was increased from 10 to 150 mA, the electro-optical conversion efficiency decreased from 49.9% to 28.8%. This result indicates that a significant portion of the efficiency reduction of the NIR pc-LED is caused by the efficiency drop of the 480 nm LED chip itself, while a relatively minor fraction is due to the thermal quenching of the phosphor. For the pc-LED based on the 5 at% phosphor, the electro-optical conversion efficiency is depicted in Fig. S5b. It exhibits a maximum NIR output power of 25.45 mW, under a drive current of 150 mA. These two pc-LEDs show similar performance, probably due to their similar external PLQYs. Using this NIR pc-LED (14 at% phosphor) as light sources, we were able to clearly visualize the distribution of blood vessels in human hands with an NIR CCD camera (Fig. 4c). The relatively long emission wavelength, the excellent PL thermal stability and high electro-optical efficiency collectively demonstrate the promising potential of the CSPO:Cr^{3+} phosphor in the application of NIR pc-LEDs.

CONCLUSIONS

In summary, we synthesized a novel broadband NIR CSPO:xCr^{3+} (x = 0, 1, 5, 10, 12, 14, 16 and 18 at%) phosphor using the high-temperature solid-phase method. This phosphor exhibited NIR light emission ranging from 725 to 1150 nm when excited by 490-nm blue light. The emission peak was observed at 875 nm with an FWHM of 140 nm. The achieved highest internal PLQY is about 49.7% for the 5 at% sample, while the highest external PLQY is about 18.4% for the 14 at% sample. Particularly, the phosphor demonstrated excellent PL thermal stability, retaining 73.5% (5 at% sample) and 64.6% (14 at% sample) of the PL intensity at 423 K compared with those at room temperature, which are the highest among the reported phosphors with emission peak exceeding 870 nm. By comparing the variable-temperature XRD data of cubic-phase CSPO:Cr^{3+} and monoclinic-phase MSPO:Cr^{3+} phosphors, it was revealed
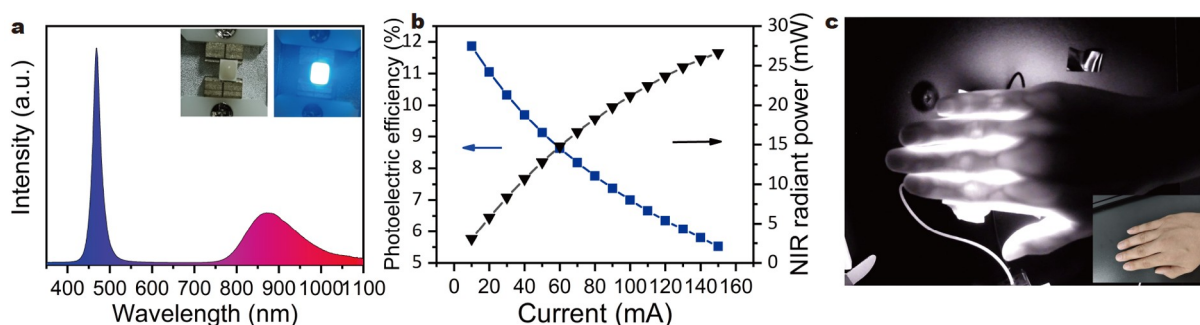

Figure 4 (a) Electroluminescence spectrum of the NIR pc-LED (14 at% phosphor) at a 150-mA drive current. Insets show the photographs of the as-fabricated NIR pc-LED and the working state of the NIR-LED. (b) NIR radiant power and photoelectric conversion efficiency as a function of drive currents of the NIR pc-LED. (c) Photographs of the human palm before and after irradiation by light emitted from the NIR pc-LED.

that the CSPO:Cr^{3+} phosphor shows much smaller bond length and bond angle variations when the temperature increased from room temperature to 423 K, which may account for its excellent PL thermal stability. Moreover, we fabricated NIR pc-LEDs by combining the CSPO:Cr^{3+} phosphor with 480-nm commercial blue chips, resulting in a maximun NIR output power of 26.62 mW. The highest electro-optical conversion efficiency is 11.87% under a drive current of 10 mA. Finally, we successfully demonstrated the application of NIR pc-LEDs in biological tissue imaging. These findings highlight the valuable potential of CSPO:Cr^{3+} phosphor for various applications, and offer insights into the screening of Cr^{3+}-doped NIR phosphor materials with exceptional PL thermal stability.

1 Saif M, Kwanten WJ, Carr JA, *et al.* Non-invasive monitoring of chronic liver disease *via* near-infrared and shortwave-infrared imaging of endogenous lipofuscin. Nat Biomed Eng, 2020, 4: 801–813

2 Manley M. Near-infrared spectroscopy and hyperspectral imaging: Non-destructive analysis of biological materials. Chem Soc Rev, 2014, 43: 8200–8214

3 Zhao F, Song Z, Liu Q. Advances in chromium-activated phosphors for near-infrared light sources. Laser & Photonics Rev, 2022, 16: 2200380

4 Vats M, Mishra S, Baghini M, *et al.* Near infrared fluorescence imaging in nano-therapeutics and photo-thermal evaluation. Int J Mol Sci, 2017, 18: 924

5 Song E, Jiang X, Zhou Y, *et al.* Heavy Mn^{2+} doped MgAl$_2$O$_4$ phosphor for high-efficient near-infrared light-emitting diode and the night-vision application. Adv Opt Mater, 2019, 7: 1901105

6 Cen H, He Y. Theory and application of near infrared reflectance spectroscopy in determination of food quality. Trends Food Sci Tech, 2007, 18: 72–83

7 Yuan L, Lin W, Zhao S, *et al.* A unique approach to development of near-infrared fluorescent sensors for *in vivo* imaging. J Am Chem Soc, 2012, 134: 13510–13523

8 Jiang H, Liu L, Yu K, *et al.* Cr^{3+}/Y^{3+} co-doped persistent luminescence nanoparticles with biological window activation for *in vivo* repeatable imaging. J Rare Earths, 2022, 40: 1389–1398

9 Guo S, Ma L, Abudureyimu M, *et al.* Improving and broadening luminescence in Gd$_{2-x}$Al$_x$GaSbO$_7$:Cr^{3+} phosphors for NIR LED applications. Inorg Chem Front, 2023, 10: 2197–2205

10 Lee H, Cho S, Lim J, *et al.* Performance comparison of tungsten-halogen light and phosphor-converted NIR LED in soluble solid content estimation of apple. Sensors, 2023, 23: 1961

11 Cai C, Liu S, Zhao F, *et al.* Inducing octahedral distortion to enhance NIR emission in Cr-doped garnet Ca$_3$(Al,Sc)$_2$Ge$_3$O$_{12}$. J Mater Chem C, 2023, 11: 8462–8469

12 He S, Zhang L, Wu H, *et al.* Efficient super broadband NIR Ca$_2$LuZr$_2$-Al$_3$O$_{12}$:Cr^{3+},Yb^{3+} garnet phosphor for pc-LED light source toward NIR spectroscopy applications. Adv Opt Mater, 2020, 8: 1901684

13 Xu X, Shao Q, Yao L, *et al.* Highly efficient and thermally stable Cr^{3+}-activated silicate phosphors for broadband near-infrared LED applications. Chem Eng J, 2020, 383: 123108

14 Sun Z, Ning Q, Zhou W, *et al.* Structural and spectroscopic investigation of an efficient and broadband NIR phosphor InBO$_3$:Cr^{3+} and its application in NIR pc-LEDs. Ceramics Int, 2021, 47: 13598–13603

15 Fang MH, Huang PY, Bao Z, *et al.* Penetrating biological tissue using light-emitting diodes with a highly efficient near-infrared ScBO$_3$:Cr^{3+} phosphor. Chem Mater, 2020, 32: 2166–2171

16 Henderson B, Imbusch GF. Optical Spectroscopy of Inorganic Solids. Oxford: Oxford University Press, 2006

17 Jia Z, Yuan C, Liu Y, *et al.* Strategies to approach high performance in Cr^{3+}-doped phosphors for high-power NIR-LED light sources. Light Sci Appl, 2020, 9: 86

18 Huang D, He X, Zhang J, *et al.* Efficient and thermally stable broadband near-infrared emission from near zero thermal expansion AlP$_3$O$_9$:Cr^{3+} phosphors. Inorg Chem Front, 2022, 9: 1692–1700

19 Huang W, Rajendran V, Chan M, *et al.* Near-infrared windows I and II phosphors for theranostic applications: Spectroscopy, bioimaging, and light-emitting diode photobiomodulation. Adv Opt Mater, 2023, 11: 2202061

20 Michel J, Liu J, Kimerling LC. High-performance Ge-on-Si photo-detectors. Nat Photon, 2010, 4: 527–534

21 Zhong J, Zhuo Y, Du F, *et al.* Efficient broadband near-infrared emission in the GaTaO$_4$:Cr^{3+} phosphor. Adv Opt Mater, 2022, 10: 2101800

22 Wang S, Pang R, Tan T, *et al.* Achieving high quantum efficiency broadband NIR Mg$_4$Ta$_2$O$_9$:Cr^{3+} phosphor through lithium-ion compensation. Adv Mater, 2023, 35: 2300124

23 Yu T, Sheng H, Chen S, *et al.* A broadband near-infrared Sc$_{1-x}$(PO$_3$)$_3$: XCr^{3+} phosphor with enhanced thermal stability and quantum yield by Yb^{3+} codoping. J Am Ceram Soc, 2022, 105: 3403–3417

24 Gao T, Zhuang W, Liu R, *et al.* Design and control of the luminescence in Cr^{3+}-doped NIR phosphors *via* crystal field engineering. J Alloys Compd, 2020, 848: 156557

25 Yao L, Shao Q, Han S, *et al.* Enhancing near-infrared photo-luminescence intensity and spectral properties in Yb^{3+} codoped LiScP$_2$O$_7$:Cr^{3+}. Chem Mater, 2020, 32: 2430–2439

26 Bagieu-Beucher M. Données cristallographiques sur deux phosphates de scandium: Sc(PO$_3$)$_3$ et Sc$_4$(P$_4$O$_{12}$)$_3$. J Appl Crystlogr, 1976, 9: 368–369

27 Shannon RD. Revised effective ionic radii and systematic studies of interatomic distances in halides and chalcogenides. Acta Cryst A, 1976, 32: 751–767

28 Yao L, Shao Q, Shi M, *et al.* Efficient ultra-broadband Ga$_4$GeO$_8$:Cr^{3+} phosphors with tunable peak wavelengths from 835 to 980 nm for NIR pc-LED application. Adv Opt Mater, 2022, 10: 2102229

29 Zhao F, Cai H, Song Z, *et al.* Structural confinement for Cr^{3+} activators toward efficient near-infrared phosphors with suppressed concentration quenching. Chem Mater, 2021, 33: 3621–3630

30 Lin Q, Wang Q, Liao M, *et al.* Trivalent chromium ions doped fluorides with both broad emission bandwidth and excellent luminescence thermal stability. ACS Appl Mater Interfaces, 2021, 13: 18274–18282

31 Liu S, Wang G, Xu L, *et al.* Synthesis and luminescence characteristics of an efficient broadband NIR phosphor: Cr^{3+} activated GaTa$_{0.5}$Nb$_{0.5}$O$_4$. Ceramics Int, 2023, 49: 33401–33406

32 Chen XH, Song EH, Zhou YY, *et al.* Distorted octahedral site occupation-induced high-efficiency broadband near-infrared emission in LiScGe$_2$O$_6$:Cr^{3+} phosphor. J Mater Chem C, 2021, 9: 13640–13646

33 Zhao M, Liu S, Cai H, *et al.* Efficient broadband near-infrared phosphor Sr$_2$ScSbO$_6$:Cr^{3+} for solar-like lighting. Sci China Mater, 2022, 65: 748–756

34 Chen XY, Zhang ZJ, Feng A, *et al.* Electronic structure, optical and thermal/concentration quenching properties of Lu$_{2-2x}$Eu$_{2x}$WO$_6$ (0≤x≤0.2). Mater Res Bull, 2015, 70: 26–31

35 Zhang H, Zhong J, Du F, *et al.* Efficient and thermally stable broadband near-infrared emission in a KAlP$_2$O$_7$:Cr^{3+} phosphor for non-destructive examination. ACS Appl Mater Interfaces, 2022, 14: 11663–11671

36 Wu Z, Han X, Zhou Y, *et al.* Efficient broadband near-infrared luminescence of Cr^{3+} doped fluoride K$_2$NaInF$_6$ and its NIR-LED application toward veins imaging. Chem Eng J, 2022, 427: 131740

37 Zhou R, Ma F, Yang Y, *et al.* Enhanced thermal stability and afterglow performance in Sr$_2$Ga$_{2-x}$Al$_x$SiO$_7$:Ce^{3+} phosphors *via* band gap tailoring. Inorg Chem Front, 2022, 9: 23–34

38 Fano U. Effects of configuration interaction on intensities and phase shifts. Phys Rev, 1961, 124: 1866–1878

39 Lempicki A, Andrews L, Nettel SJ, *et al.* Spectroscopy of Cr^{3+} in glasses: Fano antiresonances and vibronic "lamb shift". Phys Rev Lett, 1980, 44: 1234–1237

40 Tanabe Y, Sugano S. On the absorption spectra of complex ions II. J Phys Soc Jpn, 1954, 9: 766–779

41 Liu G, Molokeev MS, Xia Z. Structural rigidity control toward Cr^{3+}-based broadband near-infrared luminescence with enhanced thermal stability. Chem Mater, 2022, 34: 1376–1384

42 Dexter DL, Schulman JH. Theory of concentration quenching in inorganic phosphors. J Chem Phys, 1954, 22: 1063–1070

43 Liu S, Wang Z, Cai H, et al. Highly efficient near-infrared phosphor $LaMgGa_{11}O_{19}$:Cr^{3+}. Inorg Chem Front, 2020, 7: 1467–1473

44 Zhang L, Wang D, Liu F, et al. Minimizing bond angle distortion to improve thermal stability of Cr^{3+} doped near-infrared phosphor. Laser Photonics Rev, 2023, 17: 2300092

45 Zhang X, Chen X, Zhou C, et al. Spectral engineering and thermometric performance of $LiIn(Si_{2-x}Ge_x)O_6$:Cr^{3+} phosphor for multi-mode NIR thermometry. Ceramics Int, 2022, 48: 19484–19491

46 Baur WH. The geometry of polyhedral distortions. Predictive relationships for the phosphate group. Acta Crystlogr B Struct Sci, 1974, 30: 1195–1215

47 Robinson K, Gibbs GV, Ribbe PH. Quadratic elongation: A quantitative measure of distortion in coordination polyhedra. Science, 1971, 172: 567–570

48 Ivanovskikh KV, Ogiegło JM, Zych A, et al. Luminescence temperature quenching for Ce^{3+} and Pr^{3+} d–f emission in YAG and LuAG. ECS J Solid State Sci Technol, 2013, 2: R3148–R3152

49 Poncé S, Jia Y, Giantomassi M, et al. Understanding thermal quenching of photoluminescence in oxynitride phosphors from first principles. J Phys Chem C, 2016, 120: 4040–4047

50 Dorenbos P. Thermal quenching of Eu^{2+} 5d–4f luminescence in inorganic compounds. J Phys-Condens Matter, 2005, 17: 8103–8111

51 Amachraa M, Wang Z, Chen C, et al. Predicting thermal quenching in inorganic phosphors. Chem Mater, 2020, 32: 6256–6265

52 Liu D, Li G, Dang P, et al. Valence conversion and site reconstruction in near-infrared-emitting chromium-activated garnet for simultaneous enhancement of quantum efficiency and thermal stability. Light Sci Appl, 2023, 12: 248

53 Zhao FY, Cai H, Zhang SY, et al. Octahedron-dependent near-infrared luminescence in Cr^{3+}-activated phosphors. Mater Today Chem, 2022, 23: 100704

54 Liu G, Xia Z. Modulation of thermally stable photoluminescence in Cr^{3+}-based near-infrared phosphors. J Phys Chem Lett, 2022, 13: 5001–5008

Author contributions   Liu L and Zhu H conceived the idea; Zhu H supervised the project; Liu L carried out the materials synthesis, device fabrication, and most of the measurements. Nie W, Wu H, and Zhang J participated in part of the experiments; Liu L and Zhu H analyzed the data and charted the figures and table. Zhu H, Nie W, and Liang S revised the paper. All authors discussed the results and revised the manuscript.

Conflict of interest   The authors declare that they have no conflict of interest.

Supplementary information   Supporting data are available in the online version of the paper.

Le Liu is currently a Master degree candidate in materials and chemical engineering under the supervision of Prof. Haomiao Zhu at Fujian Normal University. His research focuses on Cr-doped oxide luminescent materials.

Haomiao Zhu is currently a professor and group leader at Fujian Institute of Research on the Structure of Matter, Chinese Academy of Sciences (FJIRSM, CAS). He earned his PhD degree from FJIRSM, CAS (2008). His research interest focuses on the syntheses, electronic structures and optical properties of inorganic luminescent materials, including lanthanide- and transition metal-doped phosphors and quantum dots, as well as their applications in lighting and display applications.

发射峰为875 nm的高热稳定性立方相 Sc(PO₃)₃:Cr³⁺荧光粉

刘乐[1,2,3], 聂文东[1,3], 吴会杰[1,3], 张景荣[1,2,3], 梁思思[1,3], 朱浩淼[1,2,3*]

摘要 近红外(NIR)荧光粉转换型发光二极管(pc-LED)具有尺寸小、效率高以及光谱易于调节的特点, 在特种照明、传感、微型近红外光谱仪等各领域有很好的应用前景. 目前, 已报道的发射波长超过850 nm的近红外荧光粉的荧光热稳定性较差. 在本项研究中, 我们合成了一种立方相结构的Sc(PO₃)₃:xCr³⁺ (x = 0, 1, 5, 10, 12, 14, 16, 18 at%)荧光粉, 其具有725–1150 nm的宽发射带, 发射峰为875 nm, 与之前报道的发射峰超过850 nm的荧光粉相比, 其表现出优异的热稳定性, 在423 K下, 5 at%样品的积分发光强度保留了室温下的73.4%. 通过对比研究立方相和单斜相 Sc(PO₃)₃:Cr³⁺荧光粉变温X射线衍射, 发现立方相荧光粉优异的荧光热稳定性可能归因于高温下较小的键长和键角变化. 利用该荧光粉制备的NIR pc-LED在150 mA电流驱动下, 产生了26.62 mW的NIR辐射功率. 驱动电流为10 mA时, 最高电光转换效率为11.87%. 这项工作为开发具有优异荧光热稳定性的Cr³⁺离子掺杂近红外荧光粉提供了思路.